frontiers | Frontiers in Materials

ORIGINAL RESEARCH
published: 14 April 2022
doi: 10.3389/fmats.2022.889499

Construction of Molybdenum Disulfide/Biological Structure Carbon Composite Photocatalysts and Their Photocatalytic Hydrogen Production

Shujing Wang[1], Jiajing Ding[1], Chencheng Wang[1], Wanfei Li[2], Zhigang Chen[1], Chengbao Liu[1] and Feng Chen[1]**

[1]School of Materials Science and Engineering, Suzhou University of Science and Technology, Suzhou, China, [2]Suzhou Key Laboratory for Nanophotonic and Nanoelectronic Materials and Its Devices, Suzhou University of Science and Technology, Suzhou, China

OPEN ACCESS

Edited by:
Zao Yi,
Southwest University of Science and Technology, China

Reviewed by:
Luhua Lu,
China University of Geosciences, China
Fei Wang,
Sichuan University, China
Yuxiang Yan,
Nanjing University, China

***Correspondence:**
Chengbao Liu
lcb@mail.usts.edu.cn
Feng Chen
ujschenfeng@163.com

Specialty section:
This article was submitted to Semiconducting Materials and Devices, a section of the journal Frontiers in Materials

Received: 04 March 2022
Accepted: 17 March 2022
Published: 14 April 2022

Citation:
Wang S, Ding J, Wang C, Li W, Chen Z, Liu C and Chen F (2022) Construction of Molybdenum Disulfide/Biological Structure Carbon Composite Photocatalysts and Their Photocatalytic Hydrogen Production. Front. Mater. 9:889499. doi: 10.3389/fmats.2022.889499

The hydrothermal calcination method using bamboo leaves as the biological template, thiourea as the sulfur source, and molybdenum chloride as the molybdenum source was employed to synthesize the molybdenum disulfide/biological structure carbon (MoS_2/C) photocatalytic composites with different concentrations of molybdenum chloride. The thermal decomposition behavior, surface morphology, phase structure, BET specific surface area, optical and photoluminescence properties, and photocatalytic activity of MoS_2/C photocatalytic composites with different concentrations of molybdenum chloride were studied. The results showed that the optimal temperature for synthesizing MoS_2/C photocatalytic composites is 700°C. Scanning electron microscopy (SEM) and transmission electron microscopy (TEM) observations show that the hydrothermal calcination method can be used to load MoS_2 onto the biological carbon and form a structurally stable composite system. Analysis of optical and photoluminescence properties shows that the MoS_2/C composites prepared by the hydrothermal calcination method with the concentration of molybdenum chloride of 0.20 mol/L exhibit a high charge transfer and separation efficiency. Photocatalytic experiments show that the MoS_2/C composites prepared by the hydrothermal calcination method with the concentration of molybdenum chloride of 0.20 mol/L have a high photocatalytic activity and cyclic stability. This excellent synthesis strategy can be used to synthesize other photocatalytic hydrogen production materials.

Keywords: hydrothermal calcination method, molybdenum disulfide, biological structure carbon, photoluminescence properties, photocatalytic activity

INTRODUCTION

With the development of world economy, non-renewable resources are gradually exhausted, so it is necessary to develop renewable resources to meet the needs of human life (Gouma et al., 2016; Wang et al., 2021a; Wang et al., 2021b; Cheng et al., 2021; Jia et al., 2021; Li et al., 2021; Zhang et al., 2021). Photocatalytic hydrogen production is an effective technology for the utilization of renewable resources and has attracted extensive attention from researchers all over the world (Kais et al., 2019; Luo et al., 2019; Ravishankar et al., 2019; Chen et al., 2019; Wang et al., 2020a). Molybdenum

disulfide (MoS_2) is a potential photocatalyst for photocatalytic decomposition of water to produce hydrogen, which has been applied in this field (Zhang et al., 2019). MoS_2 is the main component of molybdenite in nature. Block MoS_2 is made up of a large number of single or small layers of MoS_2 combined with interlayer van der Waals force and stacked. According to the different stacking modes and layers in the crystal, layered MoS_2 can be divided into three types, namely, 1T, 2H, and 3R, where the number represents the layers of the unit cell MoS_2; T, H, and R are trigonal, hexagonal, and rhombohedral, respectively (Zhang et al., 2018). 1T-MoS_2 and 3R-MoS_2 are metastable, while 2H-MoS_2 is stable and exhibits excellent semiconductor properties (Sarno and Ponticorvo, 2019).

Single or small layer MoS_2 material is a direct band gap semiconductor; its band gap width is 1.82 eV, so it can produce optical response to the visible light in the sunlight (Rumyantsev et al., 2007). However, it is easy to form folds and clusters due to the high surface activity of MoS_2 material, which greatly reduces the surface area of MoS_2 semiconductors and increases the composite probability of the photogenerated electron–hole pair. In addition, there is a significant photocorrosion effect in MoS_2 semiconductors, which limits the further improvement of photocatalytic semiconductor materials. To solve these problems, researchers put forward a variety of solutions. Yuan et al. (Qi et al., 2019) prepared MoS_2/reduced graphene oxide (rGO) composite catalytic material, whose excellent photocatalytic performance can be attributed to graphene acting as an electron transfer bridge to improve the transfer of charge carriers. Li et al. (2014) conjugated MoS_2 nanosheets to (graphite phase carbon nitride) g-C_3N_4 through an easy ultrasonic chemical method to form the MoS_2/C_3N_4 heterostructure. In this structure, MoS_2 is used as an electron trap to prolong the life of the separated electron–hole pair and can be used for the photodegradation of organic dyes. Meng and his team (Meng et al., 2013) deposited 5–20 nm p-type MoS_2 nanosheets on n-type nitrogen-doped reduced graphene oxide (N-rGO) nanosheets to form multiple p-n junctions on each rGO nanosheet. The p-MOS_2/N-rGO heterostructure greatly enhanced charge generation and inhibited charge recombination and showed high photocatalytic activity for hydrogen evolution reaction in the wavelength range from ultraviolet to near-infrared light. Generally, bamboo leaves are used as a biological template to prepare semiconductor oxide materials with a special structure, which can enhance the physical and chemical properties of the semiconductor oxide materials (Li et al., 2007; Wang et al., 2018). It is of great significance to develop a new synthesis route using bamboo leaves as biological templates to prepare MoS_2 and enhance its charge-carrier migration and separation efficiency.

In this study, we proposed to use bamboo leaves as biological templates to prepare biostructured carbon and to prepare MoS_2/biological structure carbon (C) composites with four concentration gradients by the hydrothermal calcination method. The thermal decomposition behavior, surface morphology, phase structure, BET specific surface area, optical and photoluminescence properties, and photocatalytic activity of MoS_2/C composites with different concentrations of molybdenum chloride were comparatively studied by using various instruments. Simultaneously, the cyclic stability experiment of photocatalytic hydrogen production was performed. The MoS_2/C composites prepared by the hydrothermal calcination method with the concentration of molybdenum chloride of 0.20 mol/L exhibit lowest emission intensity, high charge transfer, and separation efficiency, as well as high photocatalytic activity.

MATERIALS AND METHODS

Preparation of MoS_2/C Composite Photocatalysts

Thiourea and molybdenum chloride, with the molar ratio of 1:1, were accurately weighed. Four solutions with different concentrations of molybdenum chloride with 0.05, 0.10, 0.15, and 0.20 mol/L were prepared. The bamboo leaves are pretreated in a tubular furnace under a nitrogen atmosphere at a sintering temperature of 800°C. Four 20 g pretreated bamboo leaf biological templates were weighed and completely immersed in the aforementioned solution. After immersing for 24 h, the templates were transferred to the reaction kettle with teflon lining. The reactor was transferred to a drying oven and held at 160°C for 6 h to obtain four concentrations of precursors. The precursors were transferred to quartz tubes in a tubular furnace, and the MoS_2/C composite photocatalysts were obtained by heating the precursors from room temperature to 800°C at a rate of 5°C/min under the exposure of nitrogen protection gas.

Material Characterization

The thermogravimetric analysis (TG) and differential scanning calorimetry (DSC) of precursors were characterized by using the SDT Q600 simultaneous thermal analyzer (TA instruments, Inc. United States) under the exposure of nitrogen protection gas. The heating rate, the air flow rate, the injection volume, and the temperature range are 20 K/min, 100 ml/min, 2 mg, and 25–800°C, respectively. The microstructures of the MoS_2/C composite photocatalysts were observed by scanning electron microscopy, while the fibers and particles constituting membranes were characterized by using an Apollo 300 scanning electron microscope (SEM) and Libra 200 type transmission electron microscope (TEM) produced by Carl Zeiss IRTS, Germany. The MoS_2/C composite photocatalysts were characterized by using a Brook D8 Advance X-Ray diffractometer with the scanning angle of 20–80°, the scanning step length of 0.02°, and using Cu target Kα (λ = 0.154056 nm) radiation with the working voltage of 40 kV and current of 40 mA. UV-visible absorption spectra of the MoS_2/C composite photocatalysts were measured by using an ultraviolet and visible spectrophotometer. The fluorescence spectra of the MoS_2/C composite photocatalysts were collected in a confocal Raman system using a He-Cd laser with the RGB laser system (325 nm, NovaPro 30 mW, Germany) at room temperature. Nitrogen adsorption experiments are performed through nitrogen adsorption equipment.

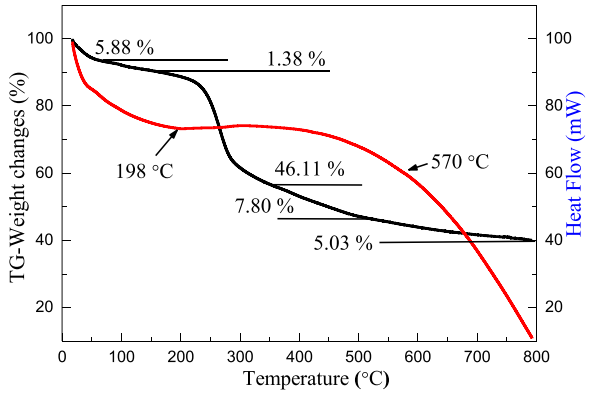

FIGURE 1 | TG–DSC curves of precursors of MoS_2/C composites with the concentrations of molybdenum chloride of 0.20 mol/L prepared by the hydrothermal calcination method.

Photocatalytic Experiments

In order to investigate the photocatalytic properties of the prepared MoS_2/C composite photocatalysts, they were applied to the reaction of photocatalytic degradation of water to produce hydrogen and compared with the pure MoS_2. The Labsolar H_2 photolysis system was developed by Beijing Perfectlight Technology Co., Ltd., and the detection device was a Shanghai Tianmei GC7900 gas chromatograph produced by Shandong Jinpu Analytical Instrument Co. Ltd., with a Microsolar 300 high-performance analog daylight xenon lamp which was used as the simulation light source. For the experiment, 100 mg sample was added to 100 ml deionized water, and sodium sulfite was added as the sacrificial agent to carry out photocatalytic hydrogen production. The hydrogen production of each material was compared after 6 h of illumination.

RESULTS AND DISCUSSION

TG-DSC Analysis

Figure 1 shows the thermogravimetry (TG) and differential scanning thermal curves (DSC) of the precursor of MoS_2/C composites with the concentrations of molybdenum chloride of 0.20 mol/L prepared by the hydrothermal calcination method. The weight loss process of the precursor is divided into five stages. As the samples were dried at 40°C, the content of free water in the precursor was slightly lower, and the weight loss ratio of free water precipitation to evaporation was 5.88% (Artiaga et al., 2005; Hsu and Lin, 2009). Hydrothermal and drying processes can effectively reduce the free water content of the precursor, and the weight loss is only 1.38% in the heating range of 100–198°C, and the release and heat dissipation of free water and bound water are energy dissipation reactions, corresponding to an obvious endothermic process on the energy curve (Saldo et al., 2002; Tahmasebi et al., 2014). The third weightless stage mainly occurs in the range of 200–400°C, which is the main concentrated range of slow thermal decomposition of cellulose (Szcześniak et al., 2008; Kristanto et al., 2021). A large number of groups in cellulose decomposition, accompanied by the pyrolysis and recombination of functional groups of lignin, and the biological structure carbon begins to generate in large quantities (Mikheeva et al., 2021). After 400°C, a small amount of cellulose cleaves to produce small molecules, the groups continue to decompose, carbon elements rearrange, and hemicellulose enters the carbonization stage and undergoes strong decomposition until 450°C basically ends (Yadav et al., 2021; Zhao et al., 2021). The main reason of 7.80% weight loss was the fracture of old bonds and the formation of new bonds in lignin. At the final weightlessness stage of the precursor, cellulose completes the carbonization reaction, and the benzene ring in lignin is first unchained and then aromatized, forming an amorphous carbon biological structure (Krueger et al., 2021; Xia et al., 2021). The hemicellulose eventually forms the biological carbon (Kabachkov et al., 2020). In addition, during the heating process of 200–570°C, the energy curve of the precursor does not decrease significantly with the pyrolysis and carbonization rearrangement of organic matter but is in dynamic equilibrium. The phenomenon can be ascribed to the release of energy, and organic carbon absorption energy of the grain growth is roughly the same, so the energy changes in a dynamic balance. Based on the analysis of weight loss in the thermal decomposition stages mentioned previously, the weight stabilizes at 800°C.

Scanning Electron Microscopy Analysis

Figures 2A–H shows the SEM images of MoS_2/C composites prepared by the hydrothermal calcination method with the different concentrations of molybdenum chloride including 0.05, 0.10, 0.15, and 0.20 mol/L at different magnifications. At low magnification, the organic matter in the leaves could be transformed into biological carbon, and the microscopic morphology of the original template was completely preserved. The composite system is based on biological structure carbon, and MoS_2 particles are loaded on the thin layer of carbon. The obtained biological structure carbon material has two main functions: First, it can provide support for the loading of MoS_2 particles so that the material can resist the deformation caused by clusters or Oswald curing during high temperature calcination and avoid the collapse phenomenon. Second, a firm bond is formed between biological carbon and MoS_2 under the action of high temperature, and the photogenerated electrons in the semiconductor are transferred to the surface of biological carbon for the reduction reaction, reducing the possibility of photogenerated electron–hole pair recombination. After the calcination process, a cluster phenomenon of MoS_2 nanoparticles was formed by the hydrothermal process under thermal action and presented a spherical structure; the diameter of spherical particles is about 2–5 μm. As the concentration of the sulfur source and molybdenum source increases in the hydrothermal process, the number of MoS_2 nanoparticles increases successively, and the cluster size increases with the concentration change. According to SEM observation, it can be inferred that the complex system has a high photocatalytic performance when

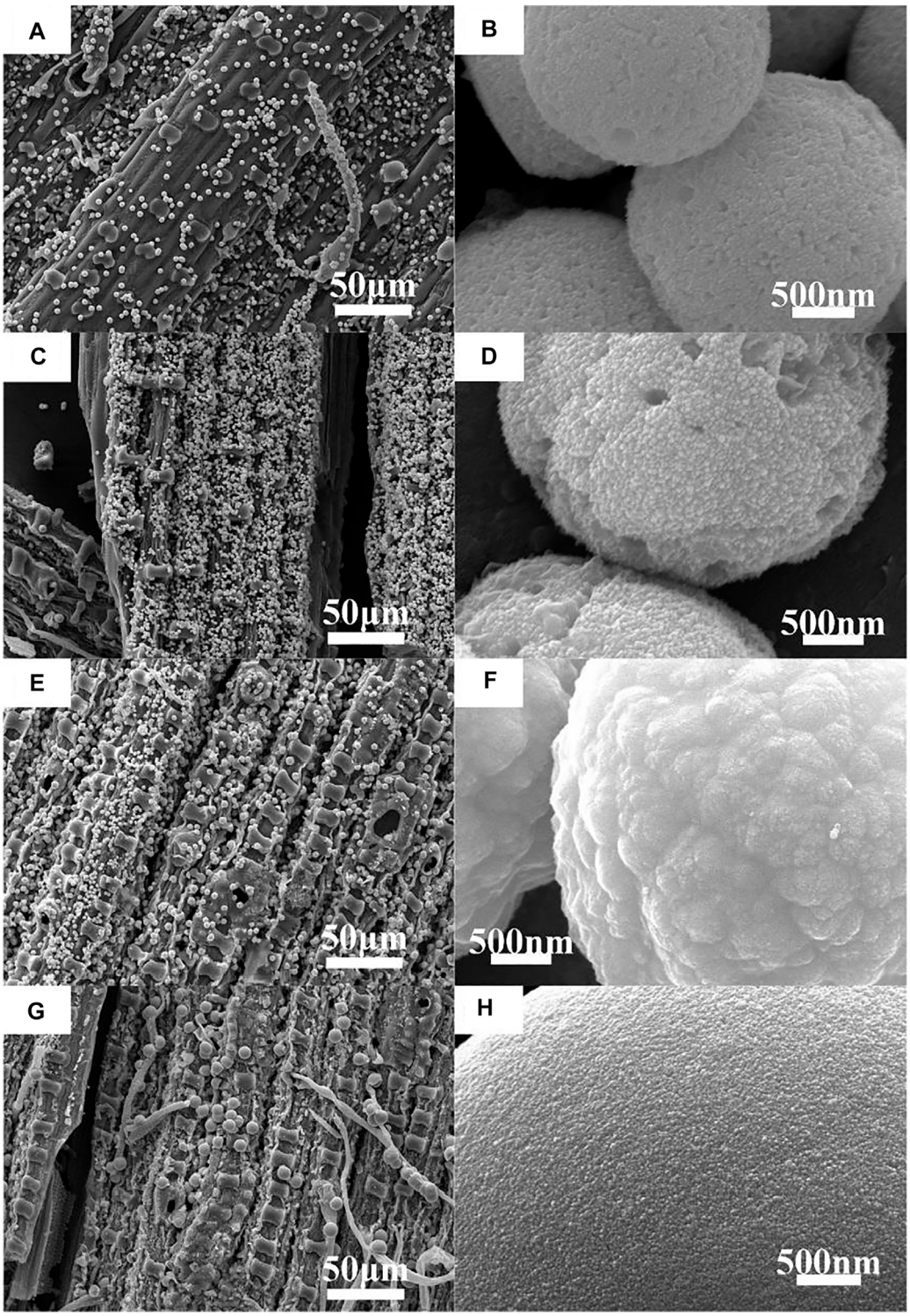

FIGURE 2 | SEM images and enlarged SEM images of MoS_2/C composites with the different concentrations of molybdenum chloride prepared by the hydrothermal calcination method. **(A,B)** 0.05 mol/L, **(C,D)** 0.10 mol/L, **(E,F)** 0.15 mol/L, and **(G,H)** 0.20 mol/L.

the molybdenum chloride concentration is 0.2 mol/L. This conclusion needs to be proven by photocatalytic experiments.

Transmission Electron Microscopy Analysis

Figure 3 shows the TEM and HRTEM images of MoS_2/C composites prepared by the hydrothermal calcination method

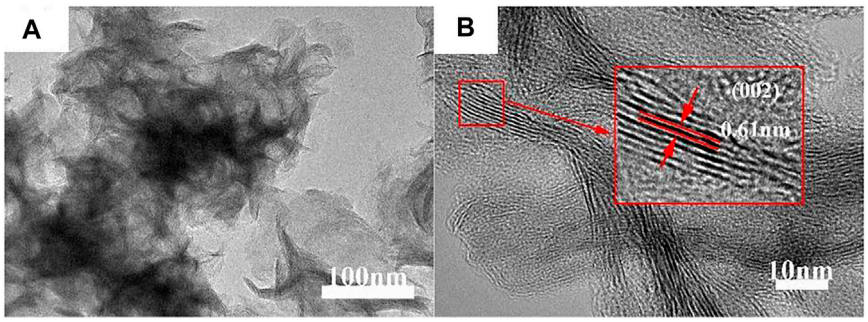

FIGURE 3 | (A) TEM and **(B)** HRTEM images of MoS_2/C composites prepared by the hydrothermal calcination method with the concentrations of molybdenum chloride of 0.20 mol/L.

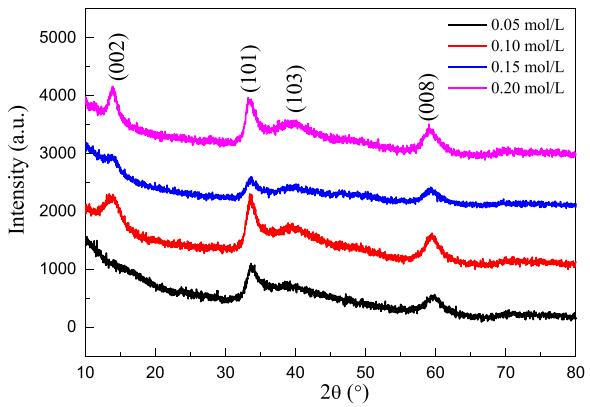

FIGURE 4 | XRD patterns of MoS_2/C composites prepared by the hydrothermal calcination method with the different concentrations of molybdenum chloride including 0.05, 0.10, 0.15, and 0.20 mol/L.

with the concentrations of molybdenum chloride of 0.20 mol/L. As can be seen from **Figure 3A**, a large number of MoS_2 nanoparticles are loaded on the a thin layer of the biological structure of carbon, indicating that the MoS_2 nanoparticles form clusters and undergo accumulation when loaded on the surface of carbon material, which is consistent with the SEM observation. **Figure 3B** was obtained by magnifying the edge of the TEM image by 10 times. From the figure, it can be found that the MoS_2 particles forming clusters are nanoscale with a particle size of about 15 nm. The crystal lattice fringe of the particles is obvious. TEM professional software is used to calculate the spacing of exposed crystal planes in the figure, and the value is 0.61 nm, corresponding to the (002) crystal plane of MoS_2 in the β-phase. Similarly, the biological structure of carbon obtained by this method is layered carbon, which further proves that high-temperature calcination is more beneficial to enhance the crystallinity of the layered carbon.

XRD Analysis

Figure 4 shows the XRD patterns of MoS_2/C composites prepared by the hydrothermal calcination method with the different concentrations of molybdenum chloride including 0.05, 0.10, 0.15, and 0.20 mol/L. A series of characteristic peaks were observed at similar locations for the four products with different concentrations, and they all corresponded to the (002), (101), (103), and (008) crystal planes of β phase MoS_2 (JCPDS card no. 41-1049) at 2θ = 13.92, 33.43, 39.77, and 59.25°, respectively. In addition, there were no redundant miscellaneous peaks in the pattern, indicating that the prepared MoS_2 nanocrystal is of high purity. The crystallinity of the material increases with the increase in the concentration, and the crystal plane with the sharpest diffraction intensity is (101). The half-peak width of the main characteristic peak of the material is wide, indicating that the average coherent scattering size of the material is small, and the concentration has no significant effect on the coherent scattering size of the material.

Optical Properties

Figure 5A shows the UV–Vis absorption spectra of molybdenum disulfide/biological structure carbon composites prepared by the hydrothermal calcination method with the different concentrations of molybdenum chloride including 0.05, 0.10, 0.15, and 0.20 mol/L. For the products obtained by the hydrothermal calcination method, the composite system absorbs all the light sources of the whole band because the color of MoS_2 is black, and the material absorbs all the light sources of the whole band. However, the composite system absorbs the infrared light source but does not respond due to the limitation of the band gap. The concentration had no significant effect on the UV–Vis absorption capacity of the composite system. The band gap energy (Eg) values of molybdenum disulfide/biological structure carbon composites were prepared by the hydrothermal calcination method with the different concentrations of molybdenum chloride including 0.05, 0.10, 0.15, and 0.20 mol/L obtained by the UV–Vis absorption spectra using the Tauc relation (Gao et al., 2018; Gao H. J. et al., 2021; Wang et al., 2021c; Wang et al., 2022) from **Figure 5B**.

$$(F(R)h\nu)^n = A\left(h\nu - E_g\right), \quad (1)$$

where ν, A, and n are the frequency, the absorption coefficient, and 2, respectively. The E_g values of molybdenum disulfide/

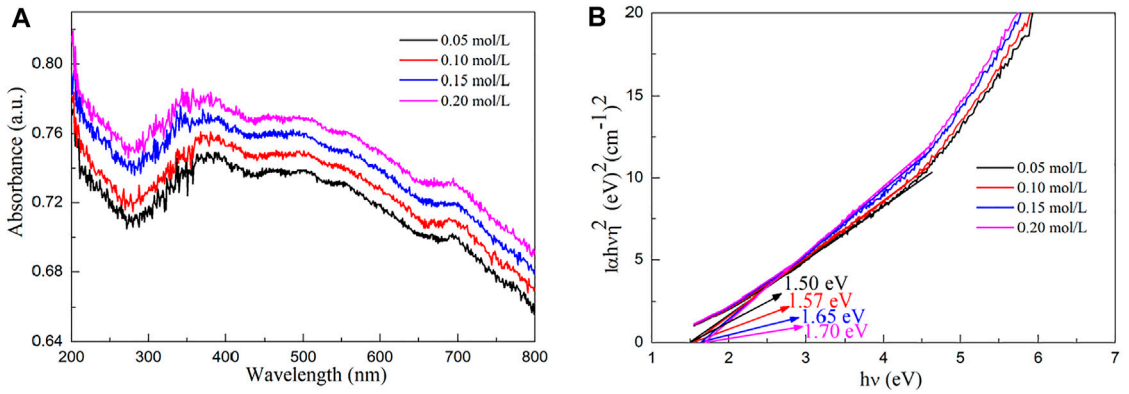

FIGURE 5 | (A) UV–Vis absorption spectra and **(B)** Eg values of molybdenum disulfide/biological structure carbon composites prepared by the hydrothermal calcination method with the different concentrations of molybdenum chloride including 0.05, 0.10, 0.15, and 0.20 mol/L.

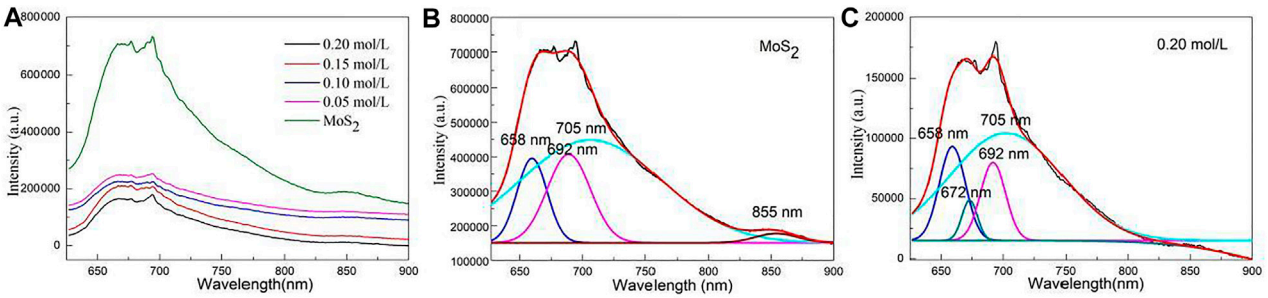

FIGURE 6 | (A) Emission spectra of MoS_2/C composites prepared by the hydrothermal calcination method with the different concentrations of molybdenum chloride including 0, 0.05, 0.10, 0.15, and 0.20 mol/L. **(B)** Emission spectrum of pure MoS_2 could be resolved into three Gaussian peaks with the maxima at 658, 692, 705, and 855 nm. **(C)** Emission spectrum of MoS_2/C composites with the concentration of molybdenum chloride of 0.20 mol/L could be resolved into four Gaussian peaks with the maxima at 658, 672, 692, and 705 nm.

biological structure carbon composites prepared by the hydrothermal calcination method with the different concentrations of molybdenum chloride including 0.05, 0.10, 0.15, and 0.20 mol/L are obtained by a simple intercept method. The Eg values of molybdenum disulfide/biological structure carbon composites prepared by the hydrothermal calcination method with the different concentrations of molybdenum chloride including 0.05, 0.10, 0.15, and 0.20 mol/L are 1.50, 1.57, 1.65, and 1.70 eV, respectively. The Eg value of molybdenum disulfide/biological structure carbon composites increases with the increasing molybdenum chlorate content. The Eg value of molybdenum disulfide/biological structure carbon composites decreases slightly than that of pure monolayer MoS_2 (1.80 eV). These results suggest that the molybdenum disulfide/biological structure carbon composites can respond to visible light.

Photoluminescence Properties

Figure 6A shows the emission spectra of MoS_2/C composites prepared by the hydrothermal calcination method with the different concentrations of molybdenum chloride including 0, 0.05, 0.10, 0.15, and 0.20 mol/L. The emission peak of pure MoS_2 is mainly concentrated in the range of 575–900 nm and has the highest emission peak intensity compared with other samples. The intensity of emission peak decreases with the increase in the molybdenum chloride content. The MoS_2/C composites prepared by the hydrothermal calcination method with the concentrations of molybdenum chloride of 0.20 mol/L have the lowest emission intensity indicating that the sample exhibits the highest charge transfer and separation efficiency. Its high charge transfer and separation efficiency result in high photocatalytic activity for splitting water to produce hydrogen.

Figure 6B shows the emission spectrum of pure MoS_2 that could be resolved into three Gaussian peaks with the maxima at 658, 692, 705, and 855 nm. The peaks at 658 and 692 nm can be ascribed to the intrinsic luminescence peak of MoS_2, which is mainly composed of the photon energy radiated by the recombination of photogenerated electron–hole pairs in the MoS_2 semiconductor. The peaks at 705 and 855 nm can be assigned to the defect luminescence peak, which is mainly composed of fluorescence radiation generated by the sulfur lattice vacancy capturing electrons in the MoS_2 semiconductor

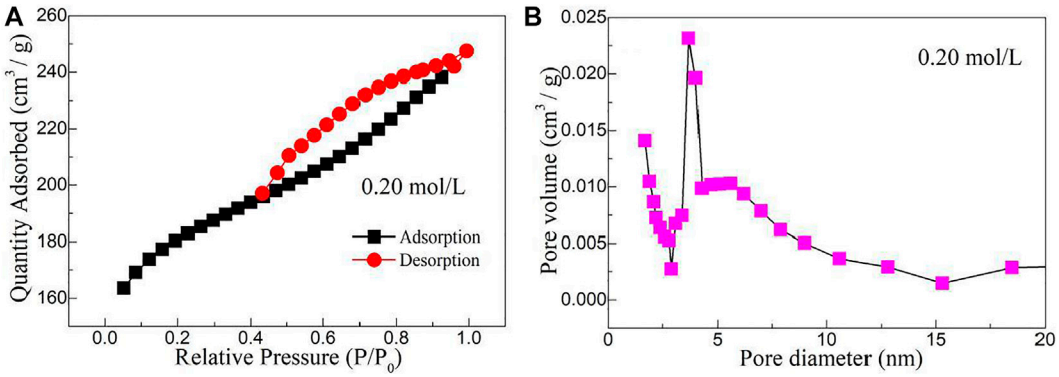

FIGURE 7 | (A) Nitrogen adsorption–desorption isotherm and **(B)** pore size distribution of molybdenum disulfide/biological structure carbon composites prepared by the hydrothermal calcination method with the concentration of molybdenum chloride of 0.20 mol/L.

and then recombination with photogenerated holes (Tang et al., 2020; Wang et al., 2020b; Wang and Tian, 2020; Gao H. et al., 2021; Wang S. F. et al., 2021).

Figure 6C shows the emission spectrum of MoS_2/C composites with the concentration of molybdenum chloride of 0.05 mol/L could be resolved into four Gaussian peaks with the maxima at 658, 672, 692, and 705 nm. This result differs from MoS_2 in two ways: one new peak at 672 nm can be observed, and the fluorescence emission peak at 855 nm is quenched. The peak at 672 nm can be ascribed to the interface defect formed by MoS_2 coupling with biological structure carbon particles. The quenching of the fluorescence emission peak at 855 nm may be due to the formation of MoS_2/C heterojunction which greatly enhances the separation and transportation of photogenerated carriers (Zhao et al., 2020; Chi et al., 2021). The intensity of the luminescent peak decreases with the increase in the content of molybdenum chloride. Generally, the charge carrier transfer and separation efficiency decrease with the increase in the luminescence intensity. The MoS_2/C composites with the concentrations of molybdenum chloride of 0.20 mol/L exhibit lowest emission intensity. Therefore, the results confirm that the MoS_2/C composites prepared by hydrothermal calcination method with the concentrations of molybdenum chloride of 0.20 mol/L have the highest charge transfer and separation efficiency.

Adsorption-Desorption Isotherm and Pore Size Distribution

Figure 7A shows the nitrogen adsorption–desorption isotherm of molybdenum disulfide/biological structure carbon composites prepared by the hydrothermal calcination method with the concentration of molybdenum chloride of 0.20 mol/L. Combined with the IUPAC classification method, the nitrogen adsorption–desorption isotherms belong to a typical type IV. When the relative pressure is at a low pressure (0–0.1), monolayer adsorption is carried out, and the adsorption capacity of the system increases gently. When the relative pressure is in the middle range (0.1–0.4), multilayer adsorption takes place, and nitrogen molecules are adsorbed on the interlayer channels of the biological structure of carbon and the slit mesopores formed by the folds of MoS_2 nanosheets. Under the relative high pressure (0.4–1.0), capillary condensation is mainly carried out in the system, and the adsorption–desorption saturation equilibrium is achieved at a p/p0 of 1.0. The H_3-type hysteresis ring formed under high pressure indicates that there are a lot of slit pore mesoporous structures formed by the accumulation of sheet MoS_2 and biological structure carbon layer in the system. Combined with the related literature studies, the causes of the H_3 hysteresis loop due to the adsorption of composite material are because of the hole wall of multilayer adsorption and condensation, two factors in the hole, by the action of the stripping process caused only by capillary condensation. Given the multilayer structure for a parallel state, Kelvin radius changes constantly, thus resulting in the H_3-type hysteresis phenomenon. The BET (Brunauer–Emmett–Teller) equation was used to analyze the data, and its specific surface area was 568.35 m^2/g. **Figure 7B** shows the pore size distribution of molybdenum disulfide/biological structure carbon composites prepared by the hydrothermal calcination method with the concentration of molybdenum chloride of 0.20 mol/L. It can be concluded from the figure that the nano-pore size of the composite is between 2 and 20 nm, which further proves that the material is a mesoporous system. It was observed that the ratio of 4 nm mesopores in the material system was high, which was caused by the coordination between pores in the carbon mesosphere of biological structure and flake MoS_2.

Photocatalytic Decomposition of Water to Produce Hydrogen

Figure 8 shows the hydrogen evolution of MoS_2/C composites prepared by the hydrothermal calcination method with the different concentrations of molybdenum chloride including 0.05, 0.10, 0.15, and 0.20 mol/L under visible light irradiation for three cycles. In addition to four samples with different concentrations of molybdenum chloride, pure MoS_2 was also tested in the photocatalytic decomposition of water to produce

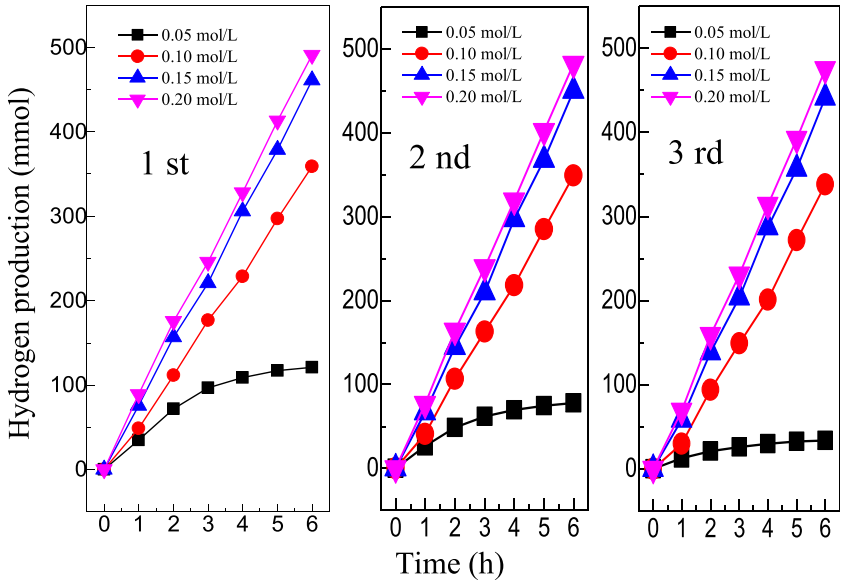

FIGURE 8 | Hydrogen evolution of MoS_2/C composites prepared by the hydrothermal calcination method with the different concentrations of molybdenum chloride including 0.05, 0.10, 0.15, and 0.20 mol/L under visible light irradiation for three cycles.

hydrogen. The experimental results show that MoS_2 can hardly decompose water to produce hydrogen. The photocatalytic performance of the composite system with a higher concentration (0.10, 0.15, and 0.20 mol/L) was better than that of the composite system with a lower concentration (0.05 mol/L) in each cycle experiment. After 6 h of illumination, the hydrogen production of low concentration MoS_2 composites tended to be gentle, while the hydrogen production of the three high concentration composites showed an upward trend. Comparing the results of three cycles, it can be found that the hydrogen production of the MoS_2 sample with the concentration of 0.05 mol/L decreases significantly with the increase of the number of cycles, while the photocatalytic hydrogen production of composite materials with other concentrations still reaches a stable high value after multiple cycles. This is because MoS_2 has a more serious photocorrosion phenomenon when the concentration is low, which limits the continuous photocatalytic reaction. After 6 h of illumination in the first cycle, the photocatalytic decomposition of hydrogen in aquatic products with four concentrations were 120.85, 358.95, 464.02, and 492.12 μmol, respectively. The hydrogen production of MoS_2/C composites prepared by the hydrothermal calcination method with the different concentrations of molybdenum chloride including 0.05, 0.10, 0.15, and 0.20 mol/L were 32.61, 336.40, 443.27, and 475.14 μmol, respectively, after 6 h of illumination in the third cycle.

Due to the low band gap value of MoS_2 and the introduction of biological structure carbon particles, the band gap value of the system is further reduced so that when the light shines on the surface of the composite material, the electrons in the MoS_2 band are easy to undergo transition to the conduction band of MoS_2 under the action of biological structure carbon (Wang and Zhao, 2019; Li et al., 2020; Deng et al., 2021; Ibrayev et al., 2021; Pu et al., 2021; Sharma et al., 2021; Syed et al., 2021; Xiu et al., 2021; Yang et al., 2021; Wang et al., 2021d). Biological structure carbon accelerates the transfer rate of charge carriers between the conduction band and the valence band of MoS_2, thus enhancing the transfer and separation efficiency of charge carriers in the system. Therefore, the photocatalytic activity of MoS_2/C composites was mainly attributed to the high charge transfer and separation efficiency of the system. The photogenerated electron in MoS_2/C composites can effectively reduce the water molecule to produce OH^- and give off H_2 (Yu et al., 2011; Zhang et al., 2013). In addition, the water molecule can be oxidized by hole to produce H^+ and to release O_2 (Zhang et al., 2013). It is also possible as the competition between the recombination of the electron–hole pair and the charge transfer and separation reaction occur in pure water. The backreaction between H_2 and O_2 produces water on the surface of MoS_2/C composites (Husin et al., 2011). The change of the band gap value continuously regulates the electron migration and recombination rate of MoS_2/C composites and then influences its hydrogen production ability.

CONCLUSION

Four kinds of MoS_2/C photocatalytic composites with different concentrations of molybdenum chloride were prepared by the hydrothermal calcination method using bamboo leaves as the biological template, thiourea as the sulfur source, and molybdenum chloride as the molybdenum source. TG-DSC, XRD, SEM, TEM, UV-VIS DRS, PL, and gas chromatograph were used to systematically study the thermal decomposition behavior, phase purity, surface morphology, optical properties, photoluminescence properties, and photocatalytic decomposition

of water to produce hydrogen of MoS_2/C photocatalytic composites with different concentrations of molybdenum chloride. The experimental results show that the hydrothermal calcination method can be used to load MoS_2 onto the biological carbon and form a structurally stable composite system. The MoS_2/C composites prepared by the hydrothermal calcination method with the concentration of molybdenum chloride of 0.20 mol/L exhibits a high charge transfer and separation efficiency. With the increase in the concentration, the photocatalytic activity of the material was significantly improved, and it showed excellent photocorrosion resistance and recyclability, which provided an effective synthesis approach for the preparation of MoS_2/C composites with a stable photocatalytic performance.

DATA AVAILABILITY STATEMENT

The original contributions presented in the study are included in the article/Supplementary Material, further inquiries can be directed to the corresponding authors.

AUTHOR CONTRIBUTIONS

SW and JD were responsible for synthesis experiments and the TG–DSC test. CW was responsible for performance tests and data analysis. WL was responsible for the analysis and guidance of XRD, SEM, and TEM. ZC was responsible for analyzing the reaction mechanism. CL and FC were responsible for the experimental design and manuscript revision.

FUNDING

This work was supported by the National Natural Science Foundation of China (21773291), the Natural Science Foundation of Jiangsu Province (BK20180103), the Qing Lan Project of Jiangsu Province, and the innovation and entrepreneurship training Program for students of the Suzhou University of Science and Technology.

REFERENCES

Artiaga, R., Naya, S., García, A., Barbadillo, F., and García, L. (2005). Subtracting the Water Effect from DSC Curves by Using Simultaneous TGA Data. *Thermochim. Acta* 428 (1-2), 137–139. doi:10.1016/j.tca.2004.11.016

Chen, Y., Li, J., and Liang, Y. (2019). Synthesis and Photocatalytic Activity of BiOBr with Different Exposed Facets and Morphology. *Russ. J. Phys. Chem.* 93 (7), 1406–1410. doi:10.1134/S0036024419070318

Cheng, T., Gao, H., Li, R., Wang, S., Yi, Z., and Yang, H. (2021). Flexoelectricity-induced Enhancement in Carrier Separation and Photocatalytic Activity of a Photocatalyst. *Appl. Surf. Sci.* 566, 150669. doi:10.1016/j.apsusc.2021.150669

Chi, Q., Zhu, G., Jia, D., Ye, W., Wang, Y., Wang, J., et al. (2021). Built-in Electric Field for Photocatalytic Overall Water Splitting through a TiO2/BiOBr P-N Heterojunction. *Nanoscale* 13 (8), 4496–4504. doi:10.1039/D0NR08928A

Deng, P., Liu, Y., Shi, L., Cui, L., Si, W., and Yao, L. (2021). Enhanced Visible-Light H2 Evolution Performance of Nitrogen Vacancy Carbon Nitride by Improving Crystallinity. *Opt. Mater.* 120, 111407. doi:10.1016/j.optmat.2021.111407

Gao, H. J., Wang, S. F., Fang, L. M., Sun, G. A., Chen, X. P., Tang, S. N., et al. (2021). Nanostructured Spinel-type M(M = Mg, Co, Zn)Cr2O4 Oxides: Novel Adsorbents for Aqueous Congo Red Removal. *Mater. Today Chem.* 22, 100593. doi:10.1016/j.mtchem.2021.100593

Gao, H., Wang, Y., Gao, Q., Pan, X., Wang, S., Yang, H., et al. (2021). Phase Evolution and Photoluminescence Behavior of MMoO4 (M = Mg, Ca, Sr) Phosphors. *Optik* 241, 167040. doi:10.1016/j.ijleo.2021.167040

Gao, H., Yang, H., Wang, S., and Zhao, X. (2018). Optical and Electrochemical Properties of Perovskite Type MAlO3 (M=Y, La, Ce) Pigments Synthesized by a Gamma-ray Irradiation Assisted Polyacrylamide Gel Route. *Ceramics Int.* 44 (12), 14754–14766. doi:10.1016/j.ceramint.2018.05.105

Gouma, P. I., Simon, S. R., and Stanacevic, M. (2016). Nano- Sensing and Catalysis Technologies for Managing Food-Water-Energy (FEW) Resources in Farming. *Mater. Today Chem.* 1-2, 40–45. doi:10.1016/j.mtchem.2016.10.004

Hsu, C.-H., and Lin, S.-Y. (2009). Rapid Examination of the Kinetic Process of Intramolecular Lactamization of Gabapentin Using DSC-FTIR. *Thermochim. Acta* 486 (1-2), 5–10. doi:10.1016/j.tca.2008.12.008

Husin, H., Su, W.-N., Chen, H.-M., Pan, C.-J., Chang, S.-H., Rick, J., et al. (2011). Photocatalytic Hydrogen Production on Nickel-Loaded LaxNa1−xTaO3 Prepared by Hydrogen Peroxide-Water Based Process. *Green. Chem.* 13 (7), 1745–1754. doi:10.1039/C1GC15070G

Ibrayev, N. K., Seliverstova, E. V., Sadykova, A. E., and Serikov, T. M. (2021). Synthesis, Structure, and Physical Properties of a Nanocomposite Based on Graphene Oxide and TiO2. *Russ. J. Phys. Chem.* 95 (4), 747–753. doi:10.1134/S0036024421040105

Jia, P., Ma, Y., Song, F., Liu, C., Hu, L., and Zhou, Y. (2021). Renewable Atom-Efficient Dendrimer-like Acetate: from Toxic Tung Oil to Non-toxic Plasticizers. *Mater. Today Chem.* 21, 100518. doi:10.1016/j.mtchem.2021.100518

Kabachkov, E. N., Kurkin, E. N., Vershinin, N. N., Balikhin, I. L., Berestenko, V. I., and Shul'ga, Y. M. (2020). Surface State of Catalysts of CO Oxidation, Obtained by Depositing Platinum on Powder of Plasma-Chemical Titanium Nitride. *Russ. J. Phys. Chem.* 94 (3), 538–543. doi:10.1134/S0036024420030127

Kais, H., Mezenner, N. Y., Trari, M., and Madjene, F. (2019). Photocatalytic Degradation of Rifampicin: Influencing Parameters and Mechanism. *Russ. J. Phys. Chem.* 93 (13), 2834–2841. doi:10.1134/S0036024419130119

Kristanto, J., Azis, M. M., and Purwono, S. (2021). Multi-distribution Activation Energy Model on Slow Pyrolysis of Cellulose and Lignin in TGA/DSC. *Heliyon* 7 (7), e07669. doi:10.1016/j.heliyon.2021.e07669

Krueger, B. C., Fowler, G. D., Templeton, M. R., and Septien, S. (2021). Faecal Sludge Pyrolysis: Understanding the Relationships between Organic Composition and thermal Decomposition. *J. Environ. Manage.* 298, 113456. doi:10.1016/j.jenvman.2021.113456

Li, B., Harlepp, S., Gensbittel, V., Wells, C. J. R., Bringel, O., Goetz, J. G., et al. (2020). Near Infra-red Light Responsive Carbon Nanotubes@mesoporous Silica for Photothermia and Drug Delivery to Cancer Cells. *Mater. Today Chem.* 17, 100308. doi:10.1016/j.mtchem.2020.100308

Li, J., Shi, X., Wang, L., and Liu, F. (2007). Synthesis of Biomorphological Mesoporous TiO2 Templated by Mimicking Bamboo Membrane in Supercritical CO2. *J. Colloid Interf. Sci.* 315 (1), 230–236. doi:10.1016/j.jcis.2007.06.065

Li, J., Wang, S., Sun, G., Gao, H., Yu, X., Tang, S., et al. (2021). Facile Preparation of MgAl2O4/CeO2/Mn3O4 Heterojunction Photocatalyst and Enhanced Photocatalytic Activity. *Mater. Today Chem.* 19, 100390. doi:10.1016/j.mtchem.2020.100390

Li, Q., Zhang, N., Yang, Y., Wang, G., and Ng, D. H. L. (2014). High Efficiency Photocatalysis for Pollutant Degradation with MoS2/C3N4 Heterostructures. *Langmuir* 30 (29), 8965–8972. doi:10.1021/la502033t

Luo, J., Yang, H., Liu, Z., Li, F., Liu, S., Ma, J., et al. (2019). Organic-inorganic Hybrid Perovskite - TiO2 Nanorod Arrays for Efficient and Stable Photoelectrochemical Hydrogen Evolution from HI Splitting. *Mater. Today Chem.* 12, 1–6. doi:10.1016/j.mtchem.2018.11.001

Meng, F., Li, J., Cushing, S. K., Zhi, M., and Wu, N. (2013). Solar Hydrogen Generation by Nanoscale P-N Junction of P-type Molybdenum Disulfide/

n-type Nitrogen-Doped Reduced Graphene Oxide. *J. Am. Chem. Soc.* 135 (28), 10286–10289. doi:10.1021/ja404851s

Mikheeva, N. N., Zaikovskii, V. I., Larichev, Y. V., and Mamontov, G. V. (2021). Toluene Abatement on Ag-CeO2/SBA-15 Catalysts: Synergistic Effect of Silver and Ceria. *Mater. Today Chem.* 21, 100530. doi:10.1016/j.mtchem.2021.100530

Pu, X., Wang, C., Chen, X., Jin, J., Li, W., and Chen, F. (2021). Synthesis and Photocatalytic Degradation of Water to Produce Hydrogen from Novel Cerium Dioxide and Silver-Doped Cerium Dioxide Fiber Membranes by the Electrospinning Method. *Front. Mater.* 8, 414. doi:10.3389/fmats.2021.776817

Qi, K., Yuan, Z., Hou, Y., Zhao, R., and Zhang, B. (2019). Facile Synthesis and Improved Li-Storage Performance of Fe-Doped MoS2/reduced Graphene Oxide as Anode Materials. *Appl. Surf. Sci.* 483, 688–695. doi:10.1016/j.apsusc.2019.04.021

Ravishankar, T. N., de O. Vaz, M., Ramakrishnappa, T., Teixeira, S. R., and Dupont, J. (2019). Ionic Liquid-Assisted Hydrothermal Synthesis of Nb/TiO2 Nanocomposites for Efficient Photocatalytic Hydrogen Production and Photodecolorization of Rhodamine B under UV-Visible and Visible Light Illuminations. *Mater. Today Chem.* 12, 373–385. doi:10.1016/j.mtchem.2019.04.001

Rumyantsev, B. M., Berendyaev, V. I., Golub', A. S., Lenenko, N. D., Novikov, Y. N., Klimenko, I. V., et al. (2007). The Role of Interface in Photo Processes in Photoconductive Heterophase Composites Based on Monolayer Dispersions of Molybdenum Disulfide. *Russ. J. Phys. Chem.* 81 (11), 1870–1876. doi:10.1134/S0036024407110271

Saldo, J., Sendra, E., and Guamis, B. (2002). Changes in Water Binding in High-Pressure Treated Cheese, Measured by TGA (Thermogravimetrical Analysis). *Innovative Food Sci. Emerging Tech.* 3 (3), 203–207. doi:10.1016/S1466-8564(02)00047-4

Sarno, M., and Ponticorvo, E. (2019). High Hydrogen Production Rate on RuS2@MoS2 Hybrid Nanocatalyst by PEM Electrolysis. *Int. J. Hydrogen Energ.* 44 (9), 4398–4405. doi:10.1016/j.ijhydene.2018.10.229

Sharma, S. K., Gupta, R., Sharma, G., Vemula, K., Koirala, A. R., Kaushik, N. K., et al. (2021). Photocatalytic Performance of Yttrium-Doped CNT-ZnO Nanoflowers Synthesized from Hydrothermal Method. *Mater. Today Chem.* 20, 100452. doi:10.1016/j.mtchem.2021.100452

Syed, A., Elgorban, A. M., and Al Kheraif, A. A. (2021). High Performance Nanohybrid CeO2@2D CdO Plates with Suppressed Charge Recombination: Insights of Photoluminescence, Visible-Light Photocatalysis, Intrinsic Mechanism and Antibacterial Activity. *Opt. Mater.* 121, 111510. doi:10.1016/j.optmat.2021.111510

Szcześniak, L., Rachocki, A., and Tritt-Goc, J. (2008). Glass Transition Temperature and thermal Decomposition of Cellulose Powder. *Cellulose* 15 (3), 445–451. doi:10.1007/s10570-007-9192-2

Tahmasebi, A., Yu, J., Su, H., Han, Y., Lucas, J., Zheng, H., et al. (2014). A Differential Scanning Calorimetric (DSC) Study on the Characteristics and Behavior of Water in Low-Rank Coals. *Fuel* 135, 243–252. doi:10.1016/j.fuel.2014.06.068

Tang, S., Wang, S., Yu, X., Gao, H., Niu, X., Wang, Y., et al. (2020). Gamma-Ray Irradiation Assisted Polyacrylamide Gel Synthesis of Scheelite Type BaWO 4 Phosphors and its Colorimetric, Optical and Photoluminescence Properties. *ChemistrySelect* 5 (34), 10599–10606. doi:10.1002/slct.202002429

Wang, B., and Zhao, B. (2019). Carbon Dots/CoFe2O4 Mesoporous Nanosphere Composites as a Magnetically Separable Visible Light Photocatalyst. *Russ. J. Phys. Chem.* 93 (2), 393–399. doi:10.1134/S0036024419020043

Wang, C., Chen, F., Tang, Y., Chen, X., Qian, J., and Chen, Z. (2018). Advanced Visible-Light Photocatalytic Property of Biologically Structured Carbon/ceria Hybrid Multilayer Membranes Prepared by Bamboo Leaves. *Ceramics Int.* 44 (6), 5834–5841. doi:10.1016/j.ceramint.2017.11.027

Wang, S., Gao, H., Sun, G., Wang, Y., Fang, L., Yang, L., et al. (2020a). Synthesis of Visible-Light-Driven SrAl2O4-Based Photocatalysts Using Surface Modification and Ion Doping. *Russ. J. Phys. Chem.* 94 (6), 1234–1247. doi:10.1134/S003602442006031X

Wang, S., Gao, H., Yu, H., Li, P., Li, Y., Chen, C., et al. (2020b). Optical and Photoluminescence Properties of the MgAl2O4:M (M = Ti, Mn, Co, Ni) Phosphors: Calcination Behavior and Photoluminescence Mechanism. *Trans. Indian Ceram. Soc.* 79 (4), 221–231. doi:10.1080/0371750X.2020.1817789

Wang, S. F., Chen, X. Y., Gao, H. J., Fang, L. M., Hu, Q. W., Sun, G. A., et al. (2021). A Comparative Study on the Phase Structure, Optical and NIR Reflectivity of BaFe12O19 Nano-Pigments by the Traditional and Modified Polyacrylamide Gel Method. *JNanoR* 67, 1–14. doi:10.4028/www.scientific.net/jnanor.67.1

Wang, S., Gao, H., Fang, L., Hu, Q., Sun, G., Chen, X., et al. (2021d). Synthesis of Novel CQDs/CeO2/SrFe12O19 Magnetic Separation Photocatalysts and Synergic Adsorption-Photocatalytic Degradation Effect for Methylene Blue Dye Removal. *Chem. Eng. J. Adv.* 6, 100089. doi:10.1016/j.ceja.2021.100089

Wang, S., Gao, H., Li, J., Wang, Y., Chen, C., Yu, X., et al. (2021b). Comparative Study of the Photoluminescence Performance and Photocatalytic Activity of CeO2/MgAl2O4 Composite Materials with an N-N Heterojunction Prepared by One-step Synthesis and Two-step Synthesis Methods. *J. Phys. Chem. Sol.* 150, 109891. doi:10.1016/j.jpcs.2020.109891

Wang, S., Tang, S., Gao, H., Chen, X., Liu, H., Yu, C., et al. (2021a). Microstructure, Optical, Photoluminescence Properties and the Intrinsic Mechanism of Photoluminescence and Photocatalysis for the BaTiO3, BaTiO3/TiO2 and BaTiO3/TiO2/CeO2 Smart Composites. *Opt. Mater.* 118, 111273. doi:10.1016/j.optmat.2021.111273

Wang, S., Tang, S., Gao, H., Fang, L., Hu, Q., Sun, G., et al. (2021c). Modified Polyacrylamide Gel Synthesis of CeO2 Nanoparticles by Using Cerium Sulfate as Metal Source and its Optical and Photoluminescence Properties. *J. Mater. Sci. Mater. Electron.* 32 (8), 10820–10834. doi:10.1007/s10854-021-05740-w

Wang, S., Tang, S., Yang, H., Wang, F., Yu, C., Gao, H., et al. (2022). A Novel Heterojunction ZnO/CuO Piezoelectric Catalysts: Fabrication, Optical Properties and Piezoelectric Catalytic Activity for Efficient Degradation of Methylene Blue. *J. Mater. Sci. Mater. Electron.* 33, 7172–7190. doi:10.1007/s10854-022-07899-2

Wang, Y., and Tian, H. (2020). Study on the Construction of YMnO3/CeO2 Composite Photocatalyst Heterostructure and Photocatalytic Degradation of Methyl Red. *Optik* 201, 163524. doi:10.1016/j.ijleo.2019.163524

Xia, M., Chen, W., Wu, J., Chen, Y., Yang, H., Chen, X., et al. (2021). Organic Salt-Assisted Pyrolysis for Preparation of Porous Carbon from Cellulose, Hemicellulose and Lignin: New Insight from Structure Evolution. *Fuel* 291, 120185. doi:10.1016/j.fuel.2021.120185

Xiu, Z., Zhang, D., and Wang, J. (2021). Direct Z-Scheme Photocatalytic System: Ag2CO3/g-C3N4 Organic-Inorganic Hybrid with Superior Activity through Built-In Electric Field Transfer Mechanism. *Russ. J. Phys. Chem.* 95 (6), 1255–1268. doi:10.1134/S0036024421060273

Yadav, N., Adolfsson, K. H., and Hakkarainen, M. (2021). Carbon Dot-Triggered Photocatalytic Degradation of Cellulose Acetate. *Biomacromolecules* 22 (5), 2211–2223. doi:10.1021/acs.biomac.1c00273

Yang, L., Wang, P. Y., and Wang, T. (2021). Performance Simulation of a 5 kW Hall Thruster. *Front. Mater.* 8, 418. doi:10.3389/fmats.2021.754479

Yu, J., Hai, Y., and Jaroniec, M. (2011). Photocatalytic Hydrogen Production over CuO-Modified Titania. *J. Colloid Interf. Sci.* 357(1), 223–228. doi:10.1016/j.jcis.2011.01.101

Zhang, F.-J., Li, X., Sun, X.-Y., Kong, C., Xie, W.-J., Li, Z., et al. (2019). Surface Partially Oxidized MoS2 Nanosheets as a Higher Efficient Cocatalyst for Photocatalytic Hydrogen Production. *Appl. Surf. Sci.* 487, 734–742. doi:10.1016/j.apsusc.2019.04.258

Zhang, P., Zhao, L., and Zhou, W. (2021). Effects of Heat Treatment on Crystallinity, Hydrophilicity, and Photocatalytic Activity of Cd0.2Zn0.8S Solid Solution. *Russ. J. Phys. Chem.* 95 (2), 262–269. doi:10.1134/S0036024421020291

Zhang, X., Du, Z., Luo, X., Sun, A., Wu, Z., and Wang, D. (2018). Template-free Fabrication of Hierarchical MoS 2/MoO 2 Nanostructures as Efficient Catalysts for Hydrogen Production. *Appl. Surf. Sci.* 433, 723–729. doi:10.1016/j.apsusc.2017.10.105

Zhang, Y. J., Liu, L. C., and Chen, D. P. (2013). Synthesis of CdS/bentonite Nanocomposite Powders for H2 Production by Photocatalytic Decomposition of Water. *Powder Techn.* 241, 7–11. doi:10.1016/j.powtec.2013.02.031

Zhao, H., Guo, L., Xing, C., Liu, H., and Li, X. (2020). A Homojunction-Heterojunction-Homojunction Scaffold Boosts Photocatalytic H2 Evolution over Cd0.5Zn0.5S/CoO Hybrids. *J. Mater. Chem. A.* 8 (4), 1955–1965. doi:10.1039/C9TA11915A

Zhao, N., Ma, H., Yao, E., Yu, Z., An, T., Zhao, F., et al. (2021). Influence of Tailored CuO and Al/CuO Nanothermites on the Thermocatalytic Degradation of Nitrocellulose and Combustion Performance of AP/HTPB Composite Propellant. *Cellulose* 28 (13), 8671–8691. doi:10.1007/s10570-021-04060-w

Conflict of Interest: The authors declare that the research was conducted in the absence of any commercial or financial relationships that could be construed as a potential conflict of interest.

Publisher's Note: All claims expressed in this article are solely those of the authors and do not necessarily represent those of their affiliated organizations, or those of the publisher, the editors, and the reviewers. Any product that may be evaluated in this article, or claim that may be made by its manufacturer, is not guaranteed or endorsed by the publisher.